

A Modality-agnostic Multi-task Foundation Model for Human Brain Imaging

Peirong Liu, Oula Puonti, Xiaoling Hu, Karthik Gopinath, Annabel Sorby-Adams
Daniel C. Alexander, W. Taylor Kimberly and Juan E. Iglesias

September 3, 2025

Abstract

Recent learning-based approaches have made astonishing advances in calibrated medical imaging like computerized tomography (CT), yet they struggle to generalize in uncalibrated modalities – notably magnetic resonance (MR) imaging, where performance is highly sensitive to the differences in MR contrast, resolution, and orientation. This prevents broad applicability to diverse real-world clinical protocols. Here we introduce **BrainFM**, a modality-agnostic, multi-task vision foundation model for human brain imaging. With the proposed “mild-to-severe” intra-subject generation and “real-synth” mix-up training strategy, **BrainFM** is resilient to the appearance of acquired images (e.g., modality, contrast, deformation, resolution, artifacts), and can be directly applied to five fundamental brain imaging tasks, including image synthesis for CT and T1w/T2w/FLAIR MRI, anatomy segmentation, scalp-to-cortical distance, bias field estimation, and registration. We evaluate the efficacy of **BrainFM** on eleven public datasets, and demonstrate its robustness and effectiveness across all tasks and input modalities. Code is available at <https://github.com/jhuldr/BrainFM>.

Keywords— Human Brain Imaging, Modality-agnostic Learning, Foundation Model

1 Introduction

Magnetic resonance imaging (MRI) enables in vivo noninvasive imaging of the human brain with exquisite and tunable soft-tissue contrast [1]. Recent machine learning based methods have achieved great improvements in faster and more accurate image analysis of brain MRI, such as image segmentation [2–6], registration [7–10], super-resolution [11, 12], and connectivity studies [13]. However, most existing MRI analysis methods are specific to certain MR contrast(s) and often require near-isotropic acquisitions. Therefore, models face

This work was primarily supported by the NIH Grant 1RF1AG080371 (Principal investigator: Juan E. Iglesias). Additional support from NIH 1RF1AG080371, 1R01EB031114, 1R01AG070988, 1RF1MH123195. ASA is funded by the American Heart Association Postdoctoral Fellowship and the Fulbright Commission. OP is supported by Lundbeckfonden R360–2021–395. Wellcome Trust award 221915/Z/20/Z and the NIHR UCLH Biomedical Research Centre support DCA on this topic.

Peirong Liu (e-mail: peirong@jhu.edu) is with the Department of Electrical and Computer Engineering at Johns Hopkins University, Baltimore, MD 21218, USA.

Xiaoling Hu, Karthik Gopinath, Annabel Sorby-Adams, W. Taylor Kimberly, and Juan E. Iglesias are with the Athinoula A. Martinos Center for Biomedical Imaging, Harvard Medical School and Massachusetts General Hospital, Boston, MA 02129, USA.

Oula Puonti is with the Danish Research Centre for Magnetic Resonance, 2650 Hvidovre, Denmark.

Daniel C. Alexander is with the Centre for Medical Image Computing, University College London, London WC1E 6BT, United Kingdom.

sharp performance drops when voxel size and anisotropy increase, or are being used for a different contrast than what seen during training [14]. This reduces model generalizability and results in duplicate data collection and training efforts given new datasets. By resorting to synthetic data, recent contrast-agnostic models [6, 15–21] achieve impressive results and largely extend the applicability of models to heterogeneous clinical acquisition protocols. However, these models are only applicable to the tasks they were trained for.

Meanwhile, task-agnostic foundation models in computer vision and natural language processing have witnessed remarkable success, fueled by fast developments in computing and large-scale datasets [22–24]. Often designed in a task-agnostic manner, foundation models have shown impressive performance in obtaining general feature representations that can be quickly adapted (e.g., finetuned) to a wide range of downstream tasks [25, 26]. However, due to different acquisition protocols, processing pipelines, and privacy requirements across institutions, assembling large-scale datasets in medical imaging requires significantly more effort than in natural language processing or computer vision. As a result, medical foundation models are not as well developed. The MONAI [27] project includes a model zoo with pretrained models for various tasks, yet they are all highly task-oriented and sensitive to specific image contrasts. Zhou et al. [28] constructed a medical foundation model, yet it is designed for the detection of eye and systemic health conditions from retinal scans, and only works on the modalities of color fundus photography and optical coherence tomography. More recently, generalist biomedical AI systems trained with vision-language data [29–31] have shown great potential in biomedical tasks, e.g., (visual) question answering, image classification, or radiology report generation and summarization. However, they have not explored challenging pixel-wise vision tasks such as reconstruction, segmentation, super-resolution, and registration.

In this work, we introduce **BrainFM**, a modality-agnostic, multi-task vision foundation model for human brain imaging.

- 1) Our on-the-fly, intra-subject data generator that can synthesize *any* contrast and resolution, with a progressive mild-to-severe scheme to randomly corrupt images during training (Fig. 1, Sec. 3.2.1). A “real-synth” mix-up strategy is further adopted to train **BrainFM** in a much more expansive and diverse space.
- 2) **BrainFM** is trained in a multi-task fashion, covering five fundamental human brain imaging tasks including: joint synthesis and super-resolution of four modalities (T1-weighted MRI, T2-weighted MRI, FLAIR MRI, and CT), anatomy segmentation, prediction of cortical distance maps, atlas registration, and bias field estimation.
- 3) We extensively evaluate **BrainFM** across all five tasks on eleven public datasets (over 5,000 images in total), including input modalities of MR (T1w, T2w, FLAIR) and CT. We further adapt **BrainFM** to hemisphere and low-field image domains, and to new downstream tasks of image super-resolution and brain age prediction. **BrainFM** achieves state-of-the-art performance in all tasks and input image modalities.

This manuscript is a significant extension of our previous conference publication, where we presented our **Brain-ID** model [32]. Specifically, we extend **Brain-ID** to **BrainFM** into a multi-task foundation model, and provide more extensive experimental evaluations from multiple aspects. (1) We introduce an improved anatomy segmentation labeling system and a “real-synth” mix-up strategy for more realistic training data generation; (2) We extend **Brain-ID** to five brain imaging tasks during pre-training, making it ready to use without additional fine-tuning effort.

2 Related work

2.1 Foundation Models in Medical Imaging

As discussed in Sec. 1, general feature representation learning in the medical imaging can be more challenging than in the natural image domain, due to limited data availability. Xu et al. [33] introduced a multiple instance learning model for feature representation in medical imaging, but it is designed specifically for classification, and only applies to histopathology images. You et al. [34] presented CVRL, a semi-supervised approach for voxel-wise representations, which is designed for image segmentation, but requires CT inputs to extract anatomical information. SAM [35] is a self-supervised framework to encode anatomical information

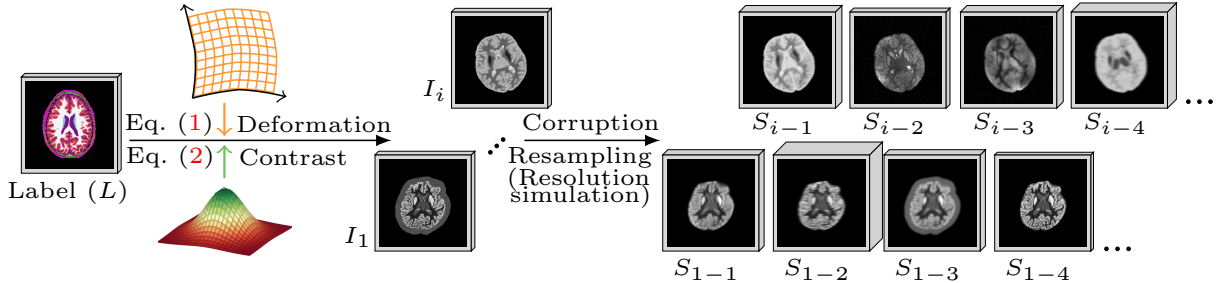


Figure 1: **BrainFM**’s data generator on the fly. Given the brain segmentation labels of a subject, we randomly generate a deformation field, and synthesize intra-subject samples featuring various contrast intensities and corruption levels (Sec. 3.1).

from CT images for feature embeddings, which has shown to be effective in downstream tasks such as registration (SAMConvex [36]). However, same as CVRL, SAM only works on CT. BrainPrint [37] is a compact and discriminative representation of brain morphology, which is specifically designed for cortical surface analyses. To the best of our knowledge, CIFL [38] is the only existing work on learning contrast-agnostic and task-independent brain feature representations. CIFL relies on contrastive learning alone, and is insufficient to outperform task/contrast-specific supervised models in downstream applications [32].

2.2 Contrast-agnostic Learning for MR Images

MRI scans acquired at different sites vary substantially in MRI contrast, resolution, and orientation. When given a new dataset, heterogeneity leads to duplicate training efforts for approaches that are sensitive to specific combinations of MR contrast, resolution, or orientation. Many classical brain segmentation models used Bayesian inference for contrast-robustness [39, 40], which requires a long processing time and struggles with low or anisotropic resolutions [6, 41]. Recently, SynthSeg [18, 20] was proposed for contrast-agnostic segmentation and achieves impressive results with a synthetic generator that simulates widely diverse contrasts. Meanwhile, there have been works with similar ideas of using synthetic data to achieve contrast-invariance in tasks like image registration [19], super-resolution [15], or skullstripping [42]. However, all the above-mentioned methods are trained in a task-specific manner, whose features therefore cannot be readily applied to other domains.

3 Method

As mentioned in Sec. 1, the main challenges to obtain a general and robust foundation model for medical imaging lie in (i) the practical restrictions of building large-scale datasets with diverse modalities and contrasts; and (ii) the nature of most medical imaging models that are task-oriented and specific to data type (modality, contrast, resolution, orientation, etc). We aim to build a general brain imaging foundation model that is:

- (i) *Robust*: the model should be robust to each subject’s distinct anatomy, unaffected by variations in image modality, contrast, poses/deformations, resolutions, or artifacts.
- (ii) *Expressive*: the well-trained model should also exhibit high expressiveness, containing rich information that facilitates easy and effective adaptation to diverse downstream tasks, eliminating the necessity for extensive training data and re-training efforts.

We first introduce **BrainFM**’s data generator (Sec. 3.1) that synthesizes a diverse range of data. Then we present our training pipeline (Sec. 3.2) for modality-agnostic multi-task learning.

3.1 Enriching the Intra-subject Learning Space

A robust representation relies on large-scale data, however, different acquisition protocols, processing pipelines, and privacy requirements across institutions make large-scale data less accessible and require significantly

more effort, e.g., via federated learning [43–45]. Moreover, only limited acquired images/modalities are usually available per subject. This lack of data consistency is a significant barrier to obtaining a robust, modality-agnostic model. **BrainFM** avoids these barriers by generating synthetic data to enrich the learning space.

To generate images with complex brain structures, we start from high-resolution brain segmentation images that provide labels of brain structures and extracerebral regions (L in Fig. 1). The generation consists of three steps, (i) deformation generation, (ii) contrast synthesis, and (iii) data corruption (including lower resolution resampling). For simplicity, Θ denotes the parameter group of the generation process described below.

3.1.1 Generating deformations

We first generate a random deformation field ($\phi|_{\theta_\phi}$) consisting of an affine transformation and a non-linear displacement field:

$$\phi|_{\theta_\phi} = \mathcal{T}|_{\theta_\phi} \circ \mathcal{A}|_{\theta_\phi}, \quad (1)$$

where $\mathcal{A}|_{\theta_\phi}$ denotes an affine transformation matrix which includes affine (rotation, scaling, shearing, translation) transformation, and $\mathcal{T}|_{\theta_\phi}$ refers to a non-linear displacement field computed as the integration of a stationary velocity field (SVF) that is smooth and invertible everywhere and thus preserves the topology of the brain anatomy. $\theta_\phi \in \Theta$ controls the transformation ranges. Further details can be found in [15].

3.1.2 Simulation of random contrast

Then, we synthesize images ($I(x)$, $x \in \Omega$) by randomly “painting” intensities on the segmentation maps according to their brain structure labels ($l \in L$). Specifically, the regional intensities are generated by separately sampling a Gaussian distribution on each labeled region:

$$\begin{cases} I(x) \sim \mathcal{N}(\mu_l, \sigma_l), & l \in L, \\ \mu_l \sim \mathcal{N}(0, 1 | \theta_\mu, \theta_l), & \sigma_l \sim \mathcal{N}(0, 1 | \theta_\sigma, \theta_l), \end{cases} \quad (2)$$

where μ_l and σ_l refer to the mean and standard deviation of each segmentation label l , and are independently sampled from Gaussian distributions at each voxel. The hyperparameters $\theta_l, \theta_\mu, \theta_\sigma \in \Theta$ control the distribution of their random values.

3.1.3 Resolution Simulation and Data Corruption

Given a deformed, contrast-synthesized image (I), we adopt the data corruption pipeline from [6], which further augments images with different levels of resolution and scanning artifacts that are commonly found in real-world clinical protocols.

3.1.4 “Real-synth” Data Mix-up

During training, we integrate real and simulated data to enhance the realism of our simulations. Specifically, we randomly mix the intensities of simulated images with those from real images, if available, acquired from the same subject, to help bridge the gap between real and simulated imaging spaces and make the generated images better reflect the actual variations and complexities present in real-world data.

As illustrated in Fig. 1, **BrainFM** can generate an infinite number of variations from a single subject with its unique brain anatomy labels. By generating images with randomized contrast/resolution/orientation on the fly for each subject, we greatly enrich the learning space to ultimately obtain a robust representation.

3.2 Modality-agnostic Multi-task Learning

As mentioned above, we would like the resulting features from **BrainFM** to be robust to intra-subject variations *and* expressive to potential downstream tasks. In this section, we introduce **BrainFM**’s learning framework to achieve these two desired properties.

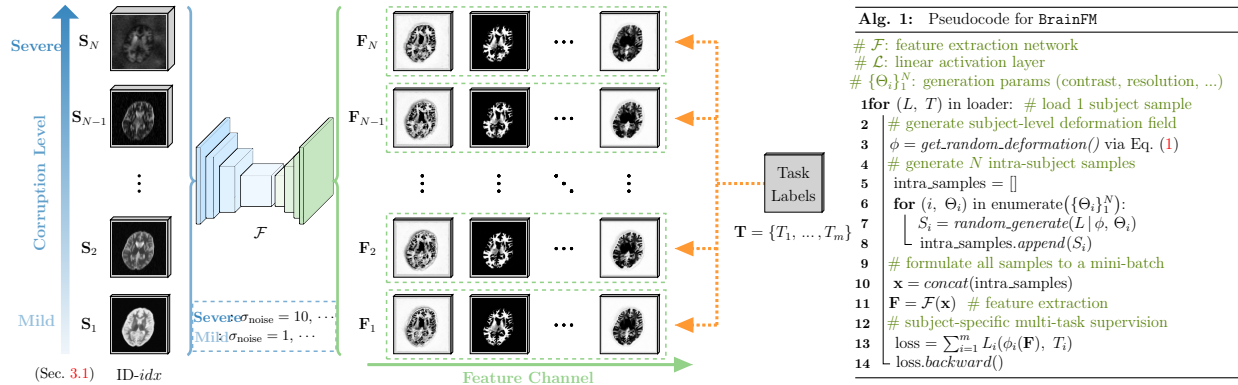


Figure 2: BrainFM’s modality-agnostic multi-task learning framework.

3.2.1 Intra-subject Data Generation

In order to learn a feature representation that is distinctive to each subject and robust to varying MR contrasts, we observe that enriching *intra*-subject samples leads to better performance (Tab. 4). Specifically, instead of including multiple subjects for a mini-batch during each training iteration as in usual practice, BrainFM focuses on maximizing the intra-subject variance to improve the subject-robustness of resulting features. As described in Alg. 1 (line 4-10), for each training iteration, after randomly selecting a subject and generating its deformation, BrainFM generates a mini-batch of intra-subject samples ($\{S_1, \dots, S_N\}$) with randomly synthesized contrasts, resolutions and corruptions (Sec. 3.1). BrainFM collects losses from all intra-subject samples and conducts back-propagation *at once*, to encourage the subject-specific robustness of its learned features.

We set the intra-subject samples within a mini-batch to have random contrasts and “mild-to-severe”, *increasing* level of corruptions (Fig. 2 (left)), to maximize the intra-subject variance while ensuring the stability of the training process against extreme corruption levels. As shown in Fig. 3, BrainFM obtains contrast/resolution-robustness that *cannot* be achieved by models trained from real images (due to the *limited variability* in their appearance), regardless of the backbone choices.

3.2.2 Multi-task Supervision

Image Synthesis For each training subject, if the ground truth modality is available, we train models to reconstruct their T1w MRI, T2w MRI, FLAIR, and CT images with the L1 loss and gradient L1 loss.

Atlas Registration To achieve a unified framework for registration, we adopt registration by regression (R2R), an atlas registration framework which predicts the atlas coordinates for every voxel of the input scan (i.e., every voxel is a keypoint) [46, 47]. We follow R2R with the L1 loss and gradient L1 loss.

Anatomy Segmentation For all training subjects, we use SynthSeg [18] to obtain the segmentation labels with 30 brain anatomical regions [40], as the gold standard segmentation target. We train models to predict the brain segmentation labels, with the soft dice loss and cross-entropy loss [18].

Distance Maps Prediction We predict distance maps to represent extracted surfaces, where each voxel encodes the shortest distance to the segmented boundary [21]. All the distance values are trained with L1 loss.

Bias Field Estimation The bias field is a smooth, low-frequency multiplicative signal that corrupts MRI images, which affects image analysis tasks such as segmentation or texture analysis [48]. Bias field estimation is often needed as a pre-processing step to correct corrupted MRI images [49]. We apply randomly

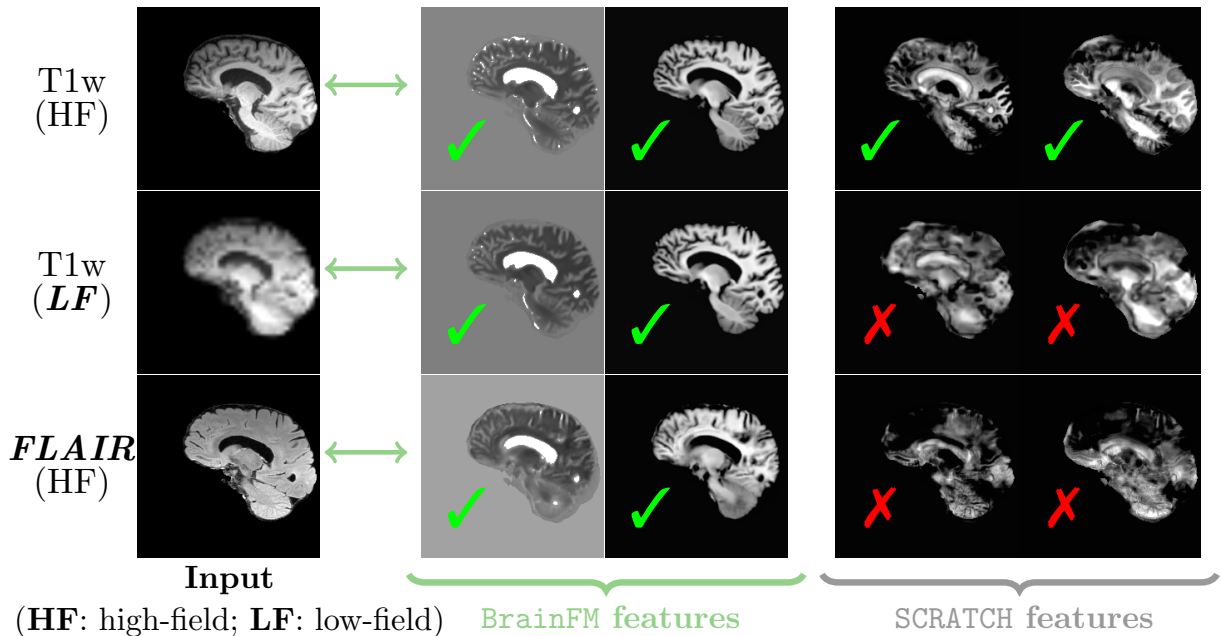


Figure 3: SCRATCH, well trained on high-field T1w scans with the same model architecture as BrainFM, produces highly descriptive features for high-field T1w images (1st row), but *does not preserve* the same high quality useful for downstream tasks when handling low-field (2nd row) or other contrasts (3rd row).

simulated bias fields to the input samples (Sec. 3.1.3), and train models with the L2 loss. Note that we pre-generate and apply the bias fields on the testing data for reproducibility, and evaluate the bias field estimation performance during inference.

4 Experiments

4.1 Datasets, Metrics, Models, Implementation Details

4.1.1 Datasets

We experience BrainFM over eleven datasets including modalities of MR and CT, the MR images further contain T1-weighted, T2-weighted, and FLAIR (fluid-attenuated inversion recovery) images.

- ABIDE [50,51]: T1-weighted (819 cases) MRI scans from the Autism Brain Imaging Data Exchange, an initiative which has aggregated functional and structural brain imaging data collected from laboratories around the world for the understanding of the neural bases of autism.
- ADHD200 [52]: T1-weighted (820 cases) MRI scans from ADHD200 Sample, a grassroots initiative dedicated to the understanding of the neural basis of Attention Deficit Hyperactivity Disorder (ADHD). We also use ADHD200 for the downstream brain age estimation task.
- ADNI3 [53]: T1-weighted (316 cases) and FLAIR (315 cases) MRI scans from ADNI3, which continues the previously funded ADNI1, ADNI-GO, and ADNI2 studies to determine the relationships between the clinical, cognitive, imaging, genetic and biochemical biomarker characteristics of the entire spectrum of sporadic late-onset AD.
- AIBL [54]: T1-weighted (646 cases), T2-weighted (302 cases), and FLAIR (273 cases) MRI scans from the Australian Imaging, Biomarkers and Lifestyle (AIBL) Study, for cognitive impairment (MCI) and Alzheimer’s disease dementia.

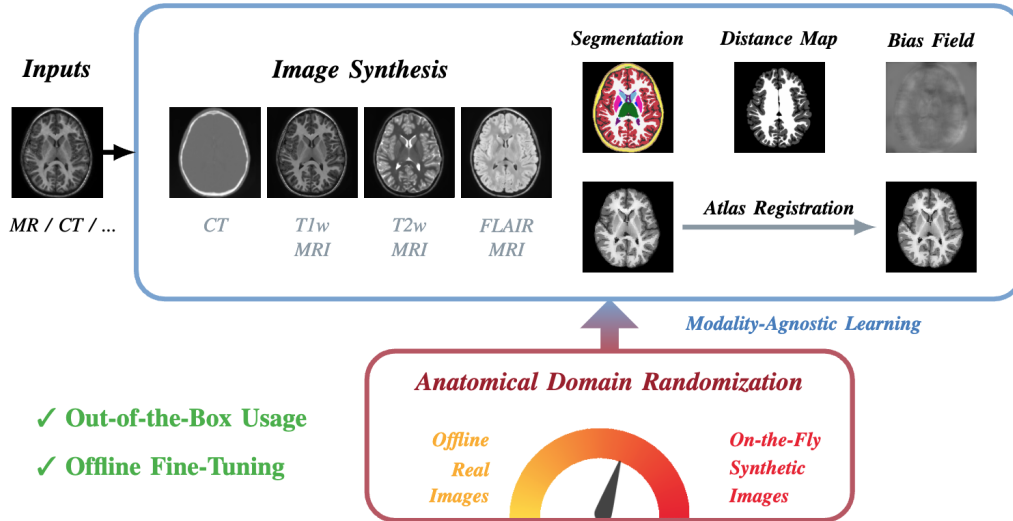


Figure 4: BrainFM’s modality-agnostic multi-task software.

- Buckner40: a subset of a larger open-access structural data set created by the Buckner lab¹. It consists of 38 T1-weighted MRI scans.
- COBRE [55]: T1-weighted (187 cases) MRI scans from the Center for Biomedical Research Excellence, including raw anatomical and functional MR data from 72 patients with Schizophrenia and 75 healthy controls.
- ISBI2015 [56]: T1-weighted (21 cases) MRI scans from the Longitudinal MS Lesion Segmentation Challenge for ISBI 2015.
- HCP [57]: T1-weighted (897 cases) and T2-weighted (897 cases) healthy MRI scans of young subjects from the Human Connectome Project, acquired at 0.7 mm resolution.
- Chinese-HCP [58]: T1-weighted (212 cases) healthy MRI scans from the Chinese Human Connectome Project, a large-scale neuroimaging project parallel to the HCP, but with a focus on the East Asian population.
- MCIC [59]: T1-weighted (161 cases) MRI scans from the schizophrenic and matched control data collection, consisting of images from schizophrenia patients and gender and age-matched controls.
- OASIS3 [60]: T1-weighted MRI (1238 cases), T2-weighted MRI (695 cases), and CT (838 cases) scans from OASIS3, which is a longitudinal neuroimaging, clinical, and cognitive dataset for normal aging and AD. We used T1-weighted MRI, T1-weighted MRI, and CT pairs with the earliest date for each subject.

Considering the potential domain gaps across datasets, we experiment with three train/test setups, to evaluate their capability better. As detailed in Tab. 1. (1) **Setup-I**, the training data includes samples from all datasets, with 10% images of each dataset randomly selected for testing; (2) **Setup-II**, the training data is from all datasets except HCP and ADNI3, that are left for testing performance on T2w and FLAIR MR. Since OASIS3 is the only dataset that includes CT images, we use the same train/test split as in **Setup-I**.; (3) **Setup-III**, in complement to **Setup-II**, **Setup-III** includes training data from all datasets except AIBL, which is left for performance testing on FLAIR. For CT, we also use the same train/test split as in **Setup-I**.

¹<https://bucknerlab.fas.harvard.edu/data-tools>

Table 1: Details on the available modalities/contrasts of each dataset, and the training/testing splits of BrainFM variants.

Setup	Split	MR			CT
		T1w	T2w	FLAIR	
	<i>Availability</i>	All	HCP OASIS3	ADNI3 AIBL	OASIS3
<i>I</i>	<i>train</i>	90% All	90% HCP 90% OASIS3	90% ADNI3 90% AIBL	90% OASIS3
	<i>test</i>	10% All	10% HCP 10% OASIS3	10% ADNI3 10% AIBL	10% OASIS3
<i>II</i>	<i>train</i>	All except HCP, ADNI3	OASIS3	AIBL	90% OASIS3
	<i>test</i>	HCP, ADNI3	HCP	ADNI3	10% OASIS3
<i>III</i>	<i>train</i>	All except AIBL	HCP	ADNI3	90% OASIS3
	<i>test</i>	AIBL	OASIS3	AIBL	10% OASIS3

4.1.2 Metrics

We evaluate individual tasks from different aspects. For image synthesis and super-resolution, we use L1, PSNR (peak signal-to-noise ratio) and SSIM. For segmentation, we use Dice scores. For atlas registration and distance map estimation, we use L1. For bias field estimation, we use the normalized L2 distance (norm-L2) to avoid possible arbitrary scalings from nonuniformity correction [49].

4.1.3 Models for Comparison

We compare performance of the above BrainFM variants with: (*i-ii*) SAMSEG [41, 61] and FastSurfer [62] (only works on T1w), state-of-the-art classical and machine-learning-based brain segmentation models, respectively; (*iii*) SynthSR [6], state-of-the-art, contrast-agnostic T1w synthesis model. We also provide fine-tuned SynthSR (SynthSR-FT) results for further comparison.

4.1.4 Data Preprocessing

For all datasets, we skull-strip all the images using SynthStrip [42], and resample them to 1 mm isotropic resolution. For all the images, except T1-weighted MRI, in each dataset, we use NiftyReg [63] rigid registration to register all images to their same-subject T1-weighted MRI counterparts. The gold-standard brain segmentation maps are obtained by performing SynthSeg [18] on the T1-weighted MR images of all the subjects. For consistency across datasets, we further masked out the de-faced regions for the datasets.

BrainFM’s synthetic generator uses (1) brain segmentation labels, for random-contrast input images generation (Sec. 3.1), and (2) randomly chosen real images for “real-synth” mix-up (Sec. 3.1.4).

4.1.5 Training

As a general feature representation model, BrainFM can use any backbone to extract brain features. For fairer comparison, we adopt the same five-level 3D UNet [2] (with 64 feature channels in the last layer). A linear regression layer is then added for each task. The training is conducted in an end-to-end fashion. We co-train BrainFM on a combination of all the real datasets listed in Sec. 4.1.1 and the synthetic images our generator (Sec. 3.1), for 2,000 epochs, with a patch size of 128^3 and a mini-batch size (i.e., number of intra-subject augmented samples) of 4. We use the synchronized AdamW optimization, with a base learning rate of 10^{-4} and a linear warm-up in the first 5 epochs, followed by a multi-step learning schedule (learning rate drops at 1,000 and 1,600 epochs) with a multiplier of 0.1.

4.2 Tasks Evaluation

In Brain-ID [32], we have validated the robustness and expressiveness properties of our anatomical domain randomization design. In this work, we particularly investigate BrainFM’s multi-task performance (Sec. 3.2.2) against (i) Brain-ID on the five tasks described in Sec. 3.2.2, to demonstrate the advantages of “real-synth” mix-up and multi-task training in BrainFM; (ii) SCRATCH: a baseline with the same data generation/architecture as Brain-ID and BrainFM, yet trained from *scratch*. SCRATCH is used to validate Brain-ID’s effectiveness;

Table 2 shows the results for image synthesis experiments, where BrainFM consistently demonstrates superior reconstruction performance over both SCRATCH and Brain-ID across all imaging modalities and training setups. Compared to SCRATCH, BrainFM markedly reduces L1 errors while substantially improving PSNR and SSIM, confirming the effectiveness of leveraging anatomical priors rather than training from scratch. Moreover, BrainFM achieves consistent gains over Brain-ID, underscoring the benefit of combining real and synthetic data during training as well as exploiting the multi-task learning setup. These improvements are evident across T1w, T2w, FLAIR MR, and CT images, suggesting that BrainFM is not only more accurate in capturing structural information, but also more robust to variations in modality. The fact that BrainFM performs reliably across three distinct experimental setups further highlights its generalizability and adaptability to heterogeneous acquisition conditions, a crucial property for practical medical imaging pipelines.

Beyond synthesis, BrainFM also provides consistent improvements in a range of downstream tasks, as shown in Table 3. For atlas registration and distance prediction, BrainFM achieves the lowest L1 errors, which translate into more precise spatial correspondences and more accurate geometric reasoning within brain anatomy. In segmentation, BrainFM yields the highest Dice scores across modalities, indicating stronger anatomical boundary delineation and more faithful recovery of fine structures compared to both baselines. For bias field estimation, BrainFM either matches or surpasses Brain-ID with lower norm-L2 errors, reflecting more reliable correction of scanner-induced intensity inhomogeneities. Collectively, these results show that BrainFM’s advantages extend beyond pure generative fidelity to tasks directly supporting quantitative neuroimaging analyses. The consistent performance gains suggest that the combination of real-synth mix-up and multi-task training fosters representations that are both data-efficient and broadly transferable, ultimately enabling a more versatile and effective framework for brain image modeling.

4.3 Additional Experiments and Further Discussions

4.3.1 Data Generation Design

As shown in Tab. 4, training with all mildly-corrupted samples results in reduced feature robustness and further harms the downstream performance, yet using all extremely corrupted samples leads to unstable training and model collapse. We train BrainFM on samples of gradually increased corruptions (Fig. 2 (left)).

4.3.2 Batch Size

BrainFM computes training loss of all intra-subject samples in a mini-batch at once (Sec. 3.2.1). We observe that larger batches improve feature robustness (Tab. 4), yet do not further enhance downstream task performances.

4.3.3 Limitations

BrainFM is designed to capture the unique anatomy of subjects, it works exceptionally well on fundamental brain imaging tasks such as reconstruction, segmentation, and super-resolution, with a simple one-layer adaption. However, as BrainFM’s data generation is solely based on anatomies, we observe that it is not adept at handling images with extensive pathology regions. Our future work will focus on contrast-agnostic, pathology-encoded representations.

5 Conclusion

We introduced **BrainFM**, a multi-task foundation model for human brain imaging, which is resilient to variations in image modalities and appearances. **BrainFM** is trained on a mix-up of synthetic and real data, and can efficiently adapt to a wide array of downstream tasks. We validated **BrainFM**'s effectiveness on eight upstream and four downstream applications, expanding across eleven public datasets with both MR and CT. **BrainFM** achieves superior performances across all tasks and modalities. We believe **BrainFM** marks the first step of modality-agnostic foundation models for neuroimaging.

References

- [1] M. N. Brant-Zawadzki, G. D. Gillan, and W. R. Nitz, "MP RAGE: A three-dimensional, T1-weighted, gradient-echo sequence—initial experience in the brain." *Radiology*, 1992. [1](#)
- [2] O. Ronneberger, P. Fischer, and T. Brox, "U-Net: Convolutional networks for biomedical image segmentation," in *MICCAI*, 2015. [1](#), [8](#)
- [3] F. Milletari, N. Navab, and S.-A. Ahmadi, "V-Net: Fully convolutional neural networks for volumetric medical image segmentation," *3DV*, 2016. [1](#)
- [4] K. Kamnitsas, C. Ledig, V. F. J. Newcombe, J. P. Simpson, A. D. Kane, D. K. Menon *et al.*, "Efficient multi-scale 3D CNN with fully connected CRF for accurate brain lesion segmentation," *Medical Image Analysis*, 2016. [1](#)
- [5] Z. Ding, X. Han, P. Liu, and M. Niethammer, "Local temperature scaling for probability calibration," in *ICCV*, 2021. [1](#)
- [6] J. E. Iglesias, B. Billot, Y. Balbastre, C. G. Magdamo, S. Arnold, S. Das *et al.*, "SynthSR: A public AI tool to turn heterogeneous clinical brain scans into high-resolution T1-weighted images for 3D morphometry," *Science Advances*, 2023. [1](#), [2](#), [3](#), [4](#), [8](#)
- [7] G. Balakrishnan, A. Zhao, M. R. Sabuncu, J. V. Guttag, and A. V. Dalca, "VoxelMorph: A learning framework for deformable medical image registration," *IEEE Transactions on Medical Imaging*, 2018. [1](#)
- [8] X. Yang, R. Kwitt, and M. Niethammer, "Quicksilver: Fast predictive image registration – a deep learning approach," *NeuroImage*, 2017. [1](#)
- [9] B. D. de Vos, F. F. Berendsen, M. A. Viergever, H. Sokooti, M. Staring, and I. Išgum, "A deep learning framework for unsupervised affine and deformable image registration," *Medical Image Analysis*, 2019. [1](#)
- [10] Z. Shen, J. Feydy, P. Liu, A. H. Curiale, R. San Jose Estepar, R. San Jose Estepar, and M. Niethammer, "Accurate point cloud registration with robust optimal transport," in *NeurIPS*, 2021. [1](#)
- [11] Q. Tian, B. Bilgiç, Q. Fan, C. Ngamsombat, N. Zaretskaya, N. E. Fultz *et al.*, "Improving in vivo human cerebral cortical surface reconstruction using data-driven super-resolution." *Cerebral Cortex*, 2020. [1](#)
- [12] R. Tanno, D. E. Worrall, E. Kaden, and D. C. Alexander, "Uncertainty modelling in deep learning for safer neuroimage enhancement: Demonstration in diffusion MRI," *NeuroImage*, 2020. [1](#)
- [13] R.-A. Müller, P. Shih, B. Keehn, J. R. Deyoe, K. M. Leyden, and D. Shukla, "Underconnected, but how? A survey of functional connectivity MRI studies in autism spectrum disorders." *Cerebral Cortex*, 2011. [1](#)
- [14] M. Wang and W. Deng, "Deep visual domain adaptation: A survey," *Neurocomputing*, 2018. [2](#)
- [15] J. E. Iglesias, B. Billot, Y. Balbastre, A. Tabari, J. Conklin, D. C. Alexander *et al.*, "Joint super-resolution and synthesis of 1 mm isotropic MP-RAGE volumes from clinical MRI exams with scans of different orientation, resolution and contrast," *NeuroImage*, 2020. [2](#), [3](#), [4](#)

- [16] P. Liu, L. Tian, Y. Zhang, S. Aylward, Y. Lee, and M. Niethammer, “Discovering hidden physics behind transport dynamics,” in *CVPR*, 2021. 2
- [17] P. Liu, Y. Lee, S. Aylward, and M. Niethammer, “Deep decomposition for stochastic normal-abnormal transport,” in *CVPR*, 2022. 2
- [18] B. Billot, D. N. Greve, O. Puonti, A. Thielscher, K. V. Leemput, B. R. Fischl *et al.*, “SynthSeg: Segmentation of brain MRI scans of any contrast and resolution without retraining,” *Medical Image Analysis*, 2021. 2, 3, 5, 8
- [19] M. Hoffmann, B. Billot, D. N. Greve, J. E. Iglesias, B. R. Fischl, and A. V. Dalca, “SynthMorph: Learning contrast-invariant registration without acquired images,” *IEEE Transactions on Medical Imaging*, 2020. 2, 3
- [20] P. Laso, S. Cerri, A. Sorby-Adams, J. Guo, F. Mateen, P. Goebel *et al.*, “Quantifying white matter hyperintensity and brain volumes in heterogeneous clinical and low-field portable MRI,” *arXiv*, vol. abs/2312.05119, 2023. 2, 3
- [21] K. Gopinath, D. N. Greve, C. Magdamo, S. Arnold, S. Das, O. Puonti, J. E. Iglesias, A. D. N. Initiative *et al.*, ““Recon-all-clinical”: Cortical surface reconstruction and analysis of heterogeneous clinical brain MRI,” *Medical Image Analysis*, 2025. 2, 5
- [22] T. Brown, B. Mann, N. Ryder, M. Subbiah, J. D. Kaplan, P. Dhariwal *et al.*, “Language models are few-shot learners,” in *NeurIPS*, 2020. 2
- [23] A. Chowdhery, S. Narang, J. Devlin, M. Bosma, G. Mishra, A. Roberts *et al.*, “PaLM: Scaling language modeling with pathways,” *JMLR*, 2022. 2
- [24] A. Kirillov, E. Mintun, N. Ravi, H. Mao, C. Rolland, L. Gustafson *et al.*, “Segment anything,” *arXiv*, vol. abs/2304.02643, 2023. 2
- [25] R. Bommasani, D. A. Hudson, E. Adeli, R. Altman, S. Arora, S. von Arx *et al.*, “On the opportunities and risks of foundation models,” *arXiv*, vol. abs/2108.07258, 2021. 2
- [26] M. Awais, M. Naseer, S. S. Khan, R. M. Anwer, H. Cholakkal, M. Shah *et al.*, “Foundational models defining a new era in vision: A survey and outlook,” *arXiv*, vol. abs/2307.13721, 2023. 2
- [27] M. J. Cardoso, W. Li, R. Brown, N. Ma, E. Kerfoot, Y. Wang *et al.*, “MONAI: An open-source framework for deep learning in healthcare,” *arXiv*, vol. abs/2211.02701, 2022. 2
- [28] Y. Zhou, M. A. Chia, S. K. Wagner, M. S. Ayhan, D. J. Williamson, R. R. Struyven *et al.*, “A foundation model for generalizable disease detection from retinal images,” *Nature*, 2023. 2
- [29] M. Moor, O. Banerjee, Z. F. H. Abad, H. M. Krumholz, J. Leskovec, E. J. Topol, and P. Rajpurkar, “Foundation models for generalist medical artificial intelligence,” *Nature*, 2023. 2
- [30] K. Singhal, S. Azizi, T. Tu, S. Mahdavi, J. Wei, H. W. Chung *et al.*, “Large language models encode clinical knowledge,” *Nature*, 2022. 2
- [31] T. Tu, S. Azizi, D. Driess, M. Schaeckermann, M. Amin, P.-C. Chang *et al.*, “Towards generalist biomedical AI,” *arXiv*, vol. abs/2307.14334, 2023. 2
- [32] P. Liu, O. Puonti, X. Hu, D. C. Alexander, and J. E. Iglesias, “Brain-ID: Learning robust feature representations for brain imaging,” in *ECCV*, 2024. 2, 3, 9
- [33] Y. Xu, T. Mo, Q. Feng, P. Zhong, M. Lai, and E. I.-C. Chang, “Deep learning of feature representation with multiple instance learning for medical image analysis,” in *ICASSP*, 2014. 2
- [34] C. You, R. Zhao, L. H. Staib, and J. S. Duncan, “Momentum contrastive voxel-wise representation learning for semi-supervised volumetric medical image segmentation,” in *MICCAI*, 2021. 2
- [35] K. Yan, J. Cai, D. Jin, S. Miao, A. P. Harrison, D. Guo *et al.*, “SAM: Self-supervised learning of pixel-wise anatomical embeddings in radiological images,” *IEEE Transactions on Medical Imaging*, 2020. 2

- [36] Z. Li, L. Tian, T. C. W. Mok, X. Bai, P. Wang, J. Ge *et al.*, “SAMConvex: Fast discrete optimization for CT registration using self-supervised anatomical embedding and correlation pyramid,” in *MICCAI*, 2023. [3](#)
- [37] C. Wachinger, P. Golland, and M. Reuter, “BrainPrint: Identifying subjects by their brain,” in *MICCAI*, 2014. [3](#)
- [38] Y. Z. R. Chua and A. V. Dalca, “Contrast invariant feature representations for segmentation and registration of medical images,” in *MIDL*, 2023. [3](#)
- [39] K. V. Leemput, F. Maes, D. Vandermeulen, and P. Suetens, “A unifying framework for partial volume segmentation of brain MR images,” *IEEE Transactions on Medical Imaging*, 2003. [3](#)
- [40] B. R. Fischl, D. H. Salat, E. Busa, M. S. Albert, M. Dieterich, C. Haselgrove *et al.*, “Whole brain segmentation automated labeling of neuroanatomical structures in the human brain,” *Neuron*, 2002. [3](#), [5](#)
- [41] O. Puonti, J. E. Iglesias, and K. V. Leemput, “Fast and sequence-adaptive whole-brain segmentation using parametric bayesian modeling,” *NeuroImage*, 2016. [3](#), [8](#)
- [42] A. Hoopes, J. S. Mora, A. V. Dalca, B. R. Fischl, and M. Hoffmann, “SynthStrip: skull-stripping for any brain image,” *NeuroImage*, 2022. [3](#), [8](#)
- [43] M. J. Sheller, B. Edwards, G. A. Reina, J. Martin, S. Pati, A. Kotrotsou *et al.*, “Federated learning in medicine: Facilitating multi-institutional collaborations without sharing patient data,” *Scientific reports*, 2020. [4](#)
- [44] M. Adnan, S. Kalra, J. C. Cresswell, G. W. Taylor, and H. R. Tizhoosh, “Federated learning and differential privacy for medical image analysis,” *Scientific reports*, 2022. [4](#)
- [45] E. Darzidehkalani, M. Ghasemi-Rad, and P. van Ooijen, “Federated learning in medical imaging: Part I: Toward multicentral health care ecosystems,” *Journal of the American College of Radiology*, 2022. [4](#)
- [46] K. Gopinath, X. Hu, M. Hoffmann, O. Puonti, and J. E. Iglesias, “Registration by regression (rbr): a framework for interpretable and flexible atlas registration,” *arXiv*, vol. abs/2404.16781, 2024. [5](#)
- [47] X. Hu, K. Gopinath, P. Liu, M. Hoffmann, K. Van Leemput, O. Puonti, and J. E. Iglesias, “Hierarchical uncertainty estimation for learning-based registration in neuroimaging,” in *ICLR*, 2025. [5](#)
- [48] J. Juntu, J. Sijbers, D. V. Dyck, and J. Gielen, “Bias field correction for MRI images,” in *CORES*, 2005. [5](#)
- [49] Z. Y. Chua, W. Zheng, M. W. L. Chee, and V. Zagorodnov, “Evaluation of performance metrics for bias field correction in MR brain images,” *Journal of Magnetic Resonance Imaging*, 2009. [5](#), [8](#)
- [50] A. Di Martino, C.-G. Yan, Q. Li, E. Denio, F. X. Castellanos, K. Alaerts *et al.*, “The autism brain imaging data exchange: towards a large-scale evaluation of the intrinsic brain architecture in autism,” *Molecular psychiatry*, 2014. [6](#)
- [51] A. Di Martino, D. O’connor, B. Chen, K. Alaerts, J. S. Anderson, M. Assaf *et al.*, “Enhancing studies of the connectome in autism using the autism brain imaging data exchange II,” *Scientific data*, 2017. [6](#)
- [52] M. R. G. Brown, G. P. S. Sidhu, R. Greiner, N. Asgarian, M. Bastani, P. H. Silverstone *et al.*, “ADHD-200 global competition: diagnosing ADHD using personal characteristic data can outperform resting state fMRI measurements,” *Frontiers in Systems Neuroscience*, 2012. [6](#)
- [53] M. W. Weiner, D. P. Veitch, P. S. Aisen, L. A. Beckett, N. J. Cairns, R. C. Green *et al.*, “The Alzheimer’s disease neuroimaging initiative 3: Continued innovation for clinical trial improvement,” *Alzheimer’s & Dementia*, 2017. [6](#)
- [54] C. Fowler, S. R. Rainey-Smith, S. Bird, J. Bomke, P. Bourgeat, B. M. Brown *et al.*, “Fifteen years of the australian imaging, biomarkers and lifestyle (AIBL) study: Progress and observations from 2,359 older adults spanning the spectrum from cognitive normality to Alzheimer’s disease,” *Journal of Alzheimer’s disease reports*, 2021. [6](#)

- [55] V. D. Calhoun, J. Sui, K. Kiehl, J. Turner, E. Allen, and G. Pearlson, “Exploring the psychosis functional connectome: aberrant intrinsic networks in schizophrenia and bipolar disorder,” *Frontiers in psychiatry*, 2012. 7
- [56] A. Carass, S. Roy, A. Jog, J. L. Cuzzocreo, E. Magrath, A. Gherman *et al.*, “Longitudinal multiple sclerosis lesion segmentation: resource and challenge,” *NeuroImage*, 2017. 7
- [57] D. C. V. Essen, K. Uğurbil, E. J. Auerbach, D. M. Barch, T. E. J. Behrens, R. D. Bucholz *et al.*, “The human connectome project: A data acquisition perspective,” *NeuroImage*, 2012. 7
- [58] N. Vogt, “The chinese human connectome project,” *Nature Methods*, 2023. 7
- [59] R. L. Gollub, J. M. Shoemaker, M. D. King, T. White, S. Ehrlich, S. R. Sponheim, V. P. Clark, J. A. Turner, B. A. Mueller, V. Magnotta *et al.*, “The MCIC collection: a shared repository of multi-modal, multi-site brain image data from a clinical investigation of schizophrenia,” *Neuroinformatics*, 2013. 7
- [60] P. J. LaMontagne, S. J. Keefe, W. Lauren, C. Xiong, E. A. Grant, K. L. Moulder *et al.*, “OASIS-3: Longitudinal neuroimaging, clinical, and cognitive dataset for normal aging and Alzheimer’s disease,” *Alzheimer’s & Dementia*, 2018. 7
- [61] S. Cerri, O. Puonti, D. S. Meier, J. Wuerfel, M. Mühlau, H. R. Siebner, and K. V. Leemput, “A contrast-adaptive method for simultaneous whole-brain and lesion segmentation in multiple sclerosis,” *NeuroImage*, 2020. 8
- [62] L. Henschel, D. Kügler, and M. Reuter, “FastSurferVINN: Building resolution-independence into deep learning segmentation methods — A solution for highres brain MRI,” *NeuroImage*, 2022. 8
- [63] M. Modat, G. R. Ridgway, Z. A. Taylor, M. Lehmann, J. Barnes, D. J. Hawkes *et al.*, “Fast free-form deformation using graphics processing units,” *Computer Methods and Programs in Biomedicine*, 2010. 8

Table 2: Comparisons of BrainFM with SCRATCH and Brain-ID, on image synthesis. Corresponding train/test setups are listed in Tab. 1. Each entry reports the metric values for L1 (\downarrow) / PSNR (\uparrow) / SSIM (\uparrow).

Setup	Model	Input \ Output	MR			CT
			T1w	T2w	FLAIR	
<i>I</i>	SCRATCH	T1w MR	0.025	0.033	0.048	70.12
	Brain-ID		0.017	0.025	0.039	67.15
	BrainFM		0.015	0.021	0.036	60.89
	SCRATCH	T2w MR	0.038	0.021	0.036	63.10
	Brain-ID		0.031	0.016	0.030	60.35
	BrainFM		0.025	0.014	0.026	56.26
	SCRATCH	FLAIR MR	0.034	0.036	0.032	-
	Brain-ID		0.028	0.029	0.026	-
	BrainFM		0.025	0.026	0.021	-
	SCRATCH	CT	0.075	0.052	-	40.25
	Brain-ID		0.061	0.045	-	37.68
	BrainFM		0.050	0.041	-	34.51
<i>II</i>	SCRATCH	T1w MR	0.026	0.035	0.049	71.02
	Brain-ID		0.019	0.028	0.040	67.31
	BrainFM		0.016	0.023	0.036	60.17
	SCRATCH	T2w MR	0.039	0.023	0.037	64.25
	Brain-ID		0.033	0.018	0.031	61.02
	BrainFM		0.027	0.015	0.028	56.92
	SCRATCH	FLAIR MR	0.035	0.038	0.033	-
	Brain-ID		0.030	0.031	0.028	-
	BrainFM		0.025	0.026	0.022	-
	SCRATCH	CT	0.076	0.054	-	41.11
	Brain-ID		0.062	0.047	-	38.72
	BrainFM		0.052	0.043	-	35.10
<i>III</i>	SCRATCH	T1w MR	0.027	0.034	0.051	71.38
	Brain-ID		0.019	0.026	0.042	67.59
	BrainFM		0.015	0.022	0.038	60.40
	SCRATCH	T2w MR	0.040	0.022	0.038	64.80
	Brain-ID		0.033	0.017	0.033	60.85
	BrainFM		0.028	0.014	0.029	57.00
	SCRATCH	FLAIR MR	0.036	0.038	0.034	-
	Brain-ID		0.030	0.031	0.029	-
	BrainFM		0.027	0.027	0.025	-
	SCRATCH	CT	0.078	0.055	-	41.42
	Brain-ID		0.064	0.047	-	37.90
	BrainFM		0.053	0.042	-	34.83

Table 3: Comparisons of BrainFM with SCRATCH and Brain-ID, on atlas registration (Reg), anatomy segmentation (Seg), distance prediction (Dist), and bias field estimation (BF). Corresponding train/test setups are listed in Tab. 1. Each entry reports the metric values of: (1) L1 (\downarrow) for Reg; (2) Dice (\uparrow) for Seg; (3) L1 (\downarrow) for Dist; and (4) norm-L2 (\downarrow) for BF.

Setup	Model	Output		Reg	Seg	Dist	BF
		Input					
<i>I</i>	SCRATCH	T1w MR		0.028	0.790	0.310	0.285
	Brain-ID			0.023	0.822	0.280	0.270
	BrainFM			0.020	0.846	0.262	0.268
	SCRATCH	T2w MR		0.025	0.795	0.320	0.292
	Brain-ID			0.019	0.822	0.284	0.281
	BrainFM			0.018	0.832	0.270	0.279
	SCRATCH	FLAIR MR		0.027	0.780	0.330	0.290
	Brain-ID			0.022	0.810	0.295	0.275
	BrainFM			0.020	0.834	0.278	0.276
	SCRATCH	CT		0.034	0.750	0.340	0.299
	Brain-ID			0.028	0.780	0.310	0.288
	BrainFM			0.026	0.802	0.294	0.286
<i>II</i>	SCRATCH	T1w MR		0.027	0.792	0.308	0.283
	Brain-ID			0.021	0.828	0.276	0.268
	BrainFM			0.019	0.850	0.260	0.267
	SCRATCH	T2w MR		0.026	0.785	0.325	0.293
	Brain-ID			0.020	0.818	0.288	0.280
	BrainFM			0.018	0.836	0.272	0.279
	SCRATCH	FLAIR MR		0.029	0.772	0.335	0.291
	Brain-ID			0.024	0.805	0.300	0.278
	BrainFM			0.022	0.829	0.284	0.276
	SCRATCH	CT		0.036	0.740	0.345	0.301
	Brain-ID			0.030	0.775	0.315	0.288
	BrainFM			0.027	0.796	0.298	0.290
<i>III</i>	SCRATCH	T1w MR		0.028	0.794	0.309	0.284
	Brain-ID			0.022	0.826	0.278	0.269
	BrainFM			0.020	0.847	0.262	0.268
	SCRATCH	T2w MR		0.026	0.788	0.322	0.294
	Brain-ID			0.019	0.820	0.285	0.282
	BrainFM			0.018	0.838	0.270	0.283
	SCRATCH	FLAIR MR		0.030	0.775	0.338	0.293
	Brain-ID			0.023	0.808	0.296	0.279
	BrainFM			0.021	0.831	0.280	0.278
	SCRATCH	CT		0.037	0.743	0.348	0.302
	Brain-ID			0.029	0.778	0.312	0.289
	BrainFM			0.027	0.800	0.296	0.290

Table 4: Comparison between BrainFM and its variants.

Model Setup <i>[Comparison Target]</i>	Feature Robustness (Intra)		Downstream (Reconstruction)		
	SSIM (\uparrow)	MS-SSIM (\uparrow)	L1 (\downarrow)	PSNR (\uparrow)	SSIM (\uparrow)
<i>[Data generation design: corruption levels in intra-subject mini-batches]</i>					
All Mild ($\sigma_{\text{noise}} = 1, \dots$)	0.792	0.813	0.028	28.30	0.960
All Medium ($\sigma_{\text{noise}} = 5, \dots$)	0.831	0.899	0.022	29.67	0.964
All Severe ($\sigma_{\text{noise}} = 10, \dots$)	N/A	N/A	N/A	N/A	N/A
Mild to Severe (BrainFM)	0.858	0.921	0.021	29.89	0.966
<i>[Mini-batch size: number of intra-subject samples]</i>					
2	0.826	0.897	0.025	28.83	0.959
3	0.841	0.902	0.022	29.30	0.962
4 (BrainFM)	0.858	0.921	0.021	29.89	0.966
5	0.860	0.929	0.021	29.93	0.965